

Alkali Metal Hydride Modification on Hydrazine Borane for Improved Dehydrogenation

Yong Shen Chua,^{*,†,‡} Qijun Pei,[§] Xiaohua Ju,[†] Wei Zhou,^{‡,||} Terrence J. Udovic,[‡] Guotao Wu,[†] Zhitao Xiong,[†] Ping Chen,^{*,†} and Hui Wu^{*,‡,||}

[†]Dalian National Laboratory for Clean Energy, Dalian Institute of Chemical Physics, Chinese Academy of Sciences, 457 Zhongshan Road, 116023, Dalian, China

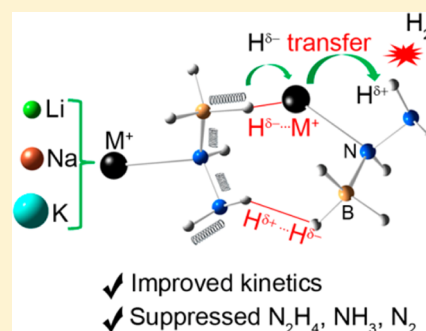
[‡]NIST Center for Neutron Research, National Institute of Standards and Technology, Gaithersburg, Maryland 20898-6102, United States

[§]School of Physical Science and Technology, Sichuan University, Chengdu 610065, China

^{||}Department of Materials Science and Engineering, University of Maryland, College Park, Maryland 20742, United States

S Supporting Information

ABSTRACT: Hydrazidotrihydridoborates of various alkali metals, i.e., $\text{NaN}_2\text{H}_3\text{BH}_3$ and $\text{KN}_2\text{H}_3\text{BH}_3$, were synthesized successfully via a liquid approach. The crystal structures of $\text{NaN}_2\text{H}_3\text{BH}_3$ and $\text{KN}_2\text{H}_3\text{BH}_3$ were determined, and their dehydrogenation properties were compared with $\text{LiN}_2\text{H}_3\text{BH}_3$ and $\text{N}_2\text{H}_4\text{BH}_3$. A clear correlation between sizes of metal cations in hydrazidotrihydridoborates and their corresponding melting and dehydrogenation temperatures was observed. The dehydrogenation temperature was found dependent on the melting temperature. Upon approaching the melting points, alkali metal hydrazidotrihydridoborates dehydrogenate rapidly in the first step, giving rise to the formation of intermediates that possess N_2BH_2 , N_2BH , and NBH_3 species. Further increasing temperature leads to the release of additional H_2 and the formation of N_2BH species. Compared to pristine $\text{N}_2\text{H}_4\text{BH}_3$, the alkali-metal-substituted hydrazidotrihydridoborates demonstrate significantly improved dehydrogenation behavior with no N_2H_4 emission and greatly suppressed NH_3 release.



INTRODUCTION

Hydrogen has been regarded as the best energy carrier for future applications due to its cleanliness. There has been a progression of energy carriers used over the past century. People began using coal (carbon) as a fuel in the 1800s during the industrial revolution. Eventually, the preferred energy carrier shifted to petroleum and more recently to natural gas, reflecting a general progression from carbon-rich to hydrogen-rich compounds. Hence, we believe that, in the near future, a further shifting from gasoline/natural gas to a cleaner and more efficient energy carrier such as hydrogen shall inevitably happen with the increasing awareness of the environmental and fossil fuel depletion issues.

It is known that when hydrogen is burnt in the air or used in a fuel cell, it produces water and energy. This process is clean because no CO_2 is released. However, hydrogen energy is sustainable only when the hydrogen production is carried out in a clean process, e.g., hydrogen from either photocatalytic water splitting or a photovoltaic/hydroelectric/wind powered electrolysis process. Moreover, for hydrogen gas use in on-board applications, a safe and efficient storage system is needed. However, development of such hydrogen storage systems is still ongoing, and hydrogen storage remains the key technical hurdle for the widespread application of hydrogen energy. Among a wide range of hydrogen storage materials, a significant

amount of research attention focuses on materials with high hydrogen capacity, e.g., complex hydrides and chemical hydrides. Ammonia borane (NH_3BH_3) is one example of a high-capacity chemical hydride hydrogen storage material, possessing 19.6 wt % of hydrogen. In order to use it for on-board applications, several approaches have been taken to improve its dehydrogenation kinetics and thermodynamics.^{1–4} Recently, hydrazine borane ($\text{N}_2\text{H}_4\text{BH}_3$), which possesses 15.4 wt % of hydrogen, was examined as a possible hydrogen storage material.⁵ However, it was reported that decomposition of $\text{N}_2\text{H}_4\text{BH}_3$ is an exothermic process, and its dehydrogenation is accompanied by emission of N_2H_4 and NH_3 .^{5–7} Inspired by the successful attempt in preparing metal amidoborane (MNH_2BH_3), Hügler et al.⁵ introduced LiH into $\text{N}_2\text{H}_4\text{BH}_3$ and found that a $\text{LiH-N}_2\text{H}_4\text{BH}_3$ mixture dehydrogenated more rapidly with 110% more capacity at 150 °C than that of $\text{N}_2\text{H}_4\text{BH}_3$. On the other hand, Wu and co-workers ball-milled LiH and $\text{N}_2\text{H}_4\text{BH}_3$ in the molar ratios of 1:1 and 1:3 and detected the formation of $\text{LiN}_2\text{H}_3\text{BH}_3$ and $\text{LiN}_2\text{H}_3\text{BH}_3 \cdot 2\text{N}_2\text{H}_4\text{BH}_3$.⁸ It was the first report of a new derivative of hydrazine borane, namely metal hydrazidotrihydridoborate. In

Received: March 2, 2014

Revised: April 22, 2014

Published: May 8, 2014

their kinetic studies, $\text{LiN}_2\text{H}_3\text{BH}_3$ demonstrated further improvement in the dehydrogenation kinetic and extent than that of $\text{LiH}-\text{N}_2\text{H}_4\text{BH}_3$ mixture under similar conditions, with great suppression of N_2H_4 and NH_3 byproducts. The improved performance was ascribed to the unique crystal chemistry of $\text{LiN}_2\text{H}_3\text{BH}_3$ with resulting variations in bonding nature and hydrogen reactivity. Moury et al.⁹ extended the chemical modification of $\text{N}_2\text{H}_4\text{BH}_3$ by using NaH. In their report, low-temperature ball milling was employed for the synthesis of $\text{NaN}_2\text{H}_3\text{BH}_3$. Our initial attempt to prepare $\text{NaN}_2\text{H}_3\text{BH}_3$ via ball milling at ambient temperature was unsuccessful. This may be due to the fact that the reaction heat generated by the interaction of NaH (a strong Lewis base) and $\text{N}_2\text{H}_4\text{BH}_3$ is sufficiently large to overcome the kinetic barrier for the decomposition of $\text{NaN}_2\text{H}_3\text{BH}_3$. In view of the highly reactivity nature of the interaction between hydrazine borane and NaH or KH, in this study, we report a facile synthesis of $\text{NaN}_2\text{H}_3\text{BH}_3$ and $\text{KN}_2\text{H}_3\text{BH}_3$ and further investigate the effect of alkali metal cations toward the dehydrogenation properties of $\text{MN}_2\text{H}_3\text{BH}_3$.

EXPERIMENTAL SECTION

$\text{N}_2\text{H}_4\text{BH}_3$ was prepared as described in ref 8. Metal hydrides used in this study are listed as follows: LiH, 98%, Alfa Aesar; NaH, 95%, Sigma-Aldrich; KH (30–35% w/w in mineral oil, Alfa Aesar, prewashed with cyclohexane). Solid-state synthesis of $\text{LiN}_2\text{H}_3\text{BH}_3$, $\text{NaN}_2\text{H}_3\text{BH}_3$, and $\text{KN}_2\text{H}_3\text{BH}_3$: A mixture of $\text{N}_2\text{H}_4\text{BH}_3$ (0.0043 mol, 0.2000 g) and LiH (0.0043 mol, 0.0355 g) was fed into a 100 mL stainless steel ball milling vessel. Four stainless steel balls were added with the ball/sample mass ratio equal to (100:1). The sample was milled at 150 rpm, in one direction for 1 min and rested for 15 s before revolved in the opposite direction, for a total of 16 h. The pressure accumulated in ball milling vessel was measured using a pressure gauge, and ball milling was progressed until no pressure increase can be detected. The gaseous product was linked to a mass spectrometer for qualitative analysis. Initial attempt in synthesizing $\text{NaN}_2\text{H}_3\text{BH}_3$ or $\text{KN}_2\text{H}_3\text{BH}_3$ using mortar and pestle was achieved by placing a small amount of $\text{N}_2\text{H}_4\text{BH}_3$ (0.000 22 mol, 0.010 g) and NaH (0.000 22 mol, 0.005 g) or KH (0.000 22 mol, 0.009 g) separately on a mortar. They were then mixed gently and homogeneously using a spatula, followed by gentle grinding using a pestle.

Wet synthesis of $\text{NaN}_2\text{H}_3\text{BH}_3$ and $\text{KN}_2\text{H}_3\text{BH}_3$: A suspension was prepared by adding 0.008 mol of metal hydrides (0.202 g of NaH or 0.337 g of KH) to 30 mL of THF in a Parr5500 autoclave reactor. $\text{N}_2\text{H}_4\text{BH}_3$ (0.008 mol, 0.368 g) was placed separately to avoid in touch with the suspension. The autoclave was then transferred carefully out of the glovebox and placed in a regulated cooling system for low-temperature synthesis. A pressure gauge was connected to the autoclave for real-time pressure recording. The inner temperature was monitored, and the stirring was initiated only when it equilibrates at desired temperature. A stirring speed of 300 rpm was kept constant throughout the synthesis until no pressure increase can be detected. The gaseous product accumulated in the autoclave was linked to mass spectrometer for qualitative analysis. Because of the fact that $\text{MN}_2\text{H}_3\text{BH}_3$ s were insoluble in THF, the insoluble product collected at the end of the reaction was filtered, and the product was washed repeatedly with 15 mL of THF for 3 times. The product was dried under dynamic vacuum for overnight to remove the remaining solvent. The dried product was then sealed in a vial and stored at low temperatures to avoid decomposition. All materials handling

was performed inside a Mbraun glovebox that was filled with He (at NIST) and argon (at DICP).

Structure Identifications. Structure identifications were carried out on PANalytical X'pert diffractometer at DICP using a homemade airtight cell and Rigaku X-ray diffractometer at NIST using 0.5 mm glass capillaries, with Cu $K\alpha$ radiation (40 kV, 40 mA). The XRD patterns were collected at room temperature in the desired 2θ range with step size of 0.026° (DICP) and 0.02° (NIST). The XRD pattern of $\text{NaN}_2\text{H}_3\text{BH}_3$ can be indexed using a monoclinic $P2_1/c$ cell with lattice parameters $a = 4.9809 \text{ \AA}$, $b = 7.9712 \text{ \AA}$, $c = 10.2607 \text{ \AA}$, and $\beta = 115.117^\circ$, whereas $\text{KN}_2\text{H}_3\text{BH}_3$'s XRD pattern can be indexed using a monoclinic $P2_1$ cell with lattice parameters $a = 6.7085 \text{ \AA}$, $b = 5.8821 \text{ \AA}$, $c = 5.7665 \text{ \AA}$, and $\beta = 108.2680^\circ$. The crystal structures were then partially solved using direct space methods. Because of the uncertain H position, first-principles molecular dynamics simulated annealing were performed to confirm the NH_2NHBH_3 . Rietveld structural refinement analyses were performed using the program GSAS.¹⁰ The $[\text{NH}_2\text{—NH—BH}_3]^-$ group was kept as a rigid body with the H—B and N—H bond lengths and bond angles constrained as the DFT calculated values due to the inadequate number of XRD observations. FTIR measurements were conducted on a Varian 3100 unit in DRIFT mode. Neutron vibrational spectra (NVS) were measured at 5 K using the BT-4 filter-analyzer neutron spectrometer (FANS) at NIST with the Cu(220) monochromator under conditions that provided energy resolutions of 2–4.5% over the vibrational energy range probed. The ^{11}B and $^1\text{H} \rightarrow ^{11}\text{B}$ cross-polarization (CP) solid state magic angle spinning nuclear magnetic resonance (MAS NMR) characterization was carried out on a Bruker AVANCE 500 MHz NMR spectrometer (11.7 T). The ^{11}B spectra was referenced to $\text{BF}_3\cdot\text{Et}_2\text{O}$ at 0 ppm.

Thermal Desorption Behavior. Open system thermal desorption behavior of the postmilled samples was investigated by using a homemade temperature-programmed desorption coupled with a mass spectrometer (TPD-MS) and thermogravimetry coupled differential thermal analysis (TG-DTA) measurements. 10 mg of sample loading was used for TPD-MS measurement. Thermogravimetry and differential thermal analysis measurement was performed on a Netsch 449C TG/DTA unit. Small sample loadings of ca. 3–5 mg were used due to sample foaming. In both open system experiments, a dynamic flow mode was employed with purified argon as a carrier gas, and the heating rate was set at $2^\circ\text{C}/\text{min}$. Closed system thermal desorption behavior of the postmilled samples was investigated by using a C80 calorimeter (Setaram) and volumetric release measurement. The C80 calorimeter allows higher sample loading (~ 50 mg). The samples were ramped with a heating rate of $0.5^\circ\text{C}/\text{min}$. The quantitative measurements of gas evolution from samples (i.e., volumetric release) were performed on a homemade Sievert-type reactor. A heating rate of $2^\circ\text{C}/\text{min}$ was used. Under a closed system, no carrier gas was used, and the gaseous product formed during the heating process was trapped in the system.

Theoretical Calculation. First-principles calculations based on density-functional theory (DFT) were performed by using the PWSCF package.¹¹ We used a Vanderbilt-type ultrasoft potential with Perdew–Burke–Ernzerhof exchange correlation. A cutoff energy of 544 eV was found to be enough for the total energy to converge within 0.5 meV/atom. Car–Parrinello molecular dynamics simulations¹² were used to help in searching for the most likely crystal structures. The conven-

tional unit cells were used, with the cell dimensions fixed at the experimental values. The initial system temperature was set to 600 K. The system was first allowed to evolve and equilibrate for 20 ps, and then the system temperature was slowly decreased to 0 K in a period of 20 ps. Structure optimizations on the resulting candidate structures at 0 K were further performed with respect to atomic positions, with the lattice parameters fixed at the experimental values. Lattice dynamics calculations were then performed on the relaxed structures using the supercell method with finite displacements¹³ to rule out unstable candidates. A $2 \times 2 \times 1$ supercell was used. The total energies of the stable candidate structures at 0 K, including corrections for the zero-point motion, were also evaluated. This information was used in combination with XRD pattern matching to derive the best crystal structure solutions of the hydrazidotrihydridoborate compounds.

RESULTS AND DISCUSSION

In this study, our initial attempt to synthesize $\text{NaN}_2\text{H}_3\text{BH}_3$ via ball milling at ambient temperature was unsuccessful due to high reactivity between NaH and $\text{N}_2\text{H}_4\text{BH}_3$. As an alternative approach, we carefully mixed and gently ground the mixture of NaH and $\text{N}_2\text{H}_4\text{BH}_3$ in a 1:1 molar ratio using mortar and pestle. This approach to synthesize $\text{NaN}_2\text{H}_3\text{BH}_3$ was successful, but separation of the side products from $\text{NaN}_2\text{H}_3\text{BH}_3$ was an issue (see Supporting Information, Figure S1). The hand-grinding approach was also attempted to synthesize $\text{KN}_2\text{H}_3\text{BH}_3$; however, a shock-sensitive reaction occurred once KH and $\text{N}_2\text{H}_4\text{BH}_3$ powders were in touch with each other, resulting in an explosive reaction. This is likely due to a stronger basicity of $\text{H}^{\delta-}$ in KH compared to NaH . The $\text{H}^{\delta-}$ in KH interacts violently with the Lewis acid $\text{H}^{\delta+}$ in $\text{N}_2\text{H}_4\text{BH}_3$, resulting in a strong exothermic reaction that further initiates the subsequent dehydrogenation of $\text{KN}_2\text{H}_3\text{BH}_3$. In order to prepare these highly reactive samples, the liquid state approach is a more viable method of synthesis. In this case, $\text{N}_2\text{H}_4\text{BH}_3$ soluble solvent (THF) was used. The solvent, on one hand, greatly alleviates the mass transport barrier induced by solid–solid interaction, allowing a more homogeneous reaction and, on the other hand, acts as a reaction medium that dissipates the reaction heat originated from the Lewis acid–base interaction.

The mixture of $\text{N}_2\text{H}_4\text{BH}_3$ and NaH or KH in 1:1 molar ratio was added into an autoclave containing 30 mL of THF and stirred under an argon atmosphere at 0 and 25 °C, respectively, until the pressure inside the reactor reached a plateau. Figure 1 shows the time dependence of pressure increase for the interactions of various metal hydrides and $\text{N}_2\text{H}_4\text{BH}_3$. For solid-

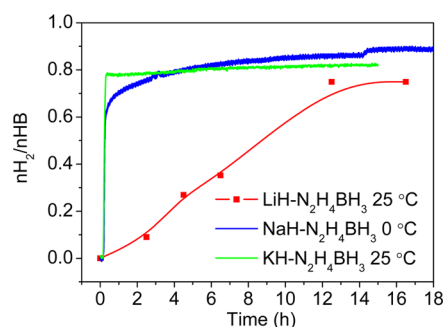
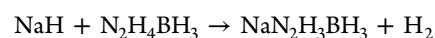
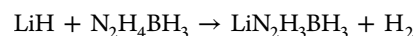


Figure 1. Time-dependent pressure increase for $\text{NaH-N}_2\text{H}_4\text{BH}_3$ and $\text{KH-N}_2\text{H}_4\text{BH}_3$ mixtures in THF solution and ball-milled $\text{LiH-N}_2\text{H}_4\text{BH}_3$.

state ball milling $\text{LiH-N}_2\text{H}_4\text{BH}_3$, the pressure increased monotonously with ball milling time. For liquid state synthesis approach, a significant pressure increase can be observed upon contacting the two starting materials, i.e., $\text{N}_2\text{H}_4\text{BH}_3$ and NaH or KH , suggesting a reaction has occurred between metal hydride and $\text{N}_2\text{H}_4\text{BH}_3$ to release gaseous products. Analysis of the gaseous product by mass spectrometer showed that H_2 is the predominant gas species (see Figure S2). Approximately 0.75, 0.85, and 0.82 mol of H_2 per mole of $\text{N}_2\text{H}_4\text{BH}_3$ were released, respectively. Taking into account the sample purity, it is suggested that the following reactions should have taken place:



It is worth pointing out that low-temperature synthesis of $\text{KN}_2\text{H}_3\text{BH}_3$ at 0 °C only resulted in 0.43 equiv of H_2 , indicating a thermodynamic controlled reaction (see Figure S3). The effort to understand the underlying reaction mechanism at low temperatures is ongoing. To allow complete reaction, synthesis of $\text{KN}_2\text{H}_3\text{BH}_3$ was carried out under ambient temperature. Upon approaching 1 equiv of H_2 , the reaction was stopped and the sample was collected for further treatment. The insoluble product formed in the reaction was filtered and washed with THF for several times. Upon separation, the product was vacuum-dried. XRD characterization of $\text{NaH-N}_2\text{H}_4\text{BH}_3$ and $\text{KH-N}_2\text{H}_4\text{BH}_3$ insoluble products showed new set of diffraction peaks which did not match with either $\text{N}_2\text{H}_4\text{BH}_3$ or metal hydrides. A pure phase was obtained in $\text{NaH-N}_2\text{H}_4\text{BH}_3$, while remaining of a small amount of KH was detected in the $\text{KH-N}_2\text{H}_4\text{BH}_3$ sample (Figure S4). The new phase obtained from the interaction of NaH and $\text{N}_2\text{H}_4\text{BH}_3$ can be indexed using a monoclinic cell with a space group of $P2_1/c$ and with lattice constants of $a = 4.9809 \text{ \AA}$, $b = 7.9712 \text{ \AA}$, $c = 10.2607 \text{ \AA}$, and $\beta = 115.117^\circ$, which agrees with the recently reported structure of $\text{NaN}_2\text{H}_3\text{BH}_3$ prepared by low-temperature ball milling.⁵ For the new phase from $\text{KH-N}_2\text{H}_4\text{BH}_3$, it can be indexed using a different monoclinic cell with the space group $P2_1$ and with lattice constants of $a = 6.7085 \text{ \AA}$, $b = 5.8821 \text{ \AA}$, $c = 5.7665 \text{ \AA}$, and $\beta = 108.268^\circ$. Rietveld refinements of the $\text{NaN}_2\text{H}_3\text{BH}_3$ and $\text{KN}_2\text{H}_3\text{BH}_3$ optimal structures determined from combined direct space methods and first-principles molecular dynamics simulated annealing yielded excellent fits with the agreement factors of $R_{wp} = 0.0601$ and 0.0388 and $R_p = 0.0432$ and 0.0277 , respectively (see Figures S5 and S6). The detailed structural information is given in Tables S1 and S2. Noted that the refinement based on laboratory X-ray data cannot provide highly accurate atomic coordinates, especially for H. First-principles calculations were thus performed, and the fully relaxed structure is used in the bond length discussion below. In addition, NVS (see Figure 2) analyses of $\text{NaN}_2\text{H}_3\text{BH}_3$ and $\text{KN}_2\text{H}_3\text{BH}_3$ further confirm the validity of the proposed structures. For comparison purposes, $\text{LiN}_2\text{H}_3\text{BH}_3$ was prepared via ball milling LiH and $\text{N}_2\text{H}_4\text{BH}_3$ in the molar ratio of 1 to 1.

From the thermodynamic point of view, the formations of $\text{LiN}_2\text{H}_3\text{BH}_3$, $\text{NaN}_2\text{H}_3\text{BH}_3$, and $\text{KN}_2\text{H}_3\text{BH}_3$ are energetically favorable. The highly exothermic reaction between metal hydride and $\text{N}_2\text{H}_4\text{BH}_3$ during the synthesis suggests that $\text{MN}_2\text{H}_3\text{BH}_3$ is thermodynamically stable. Figure 3 shows the

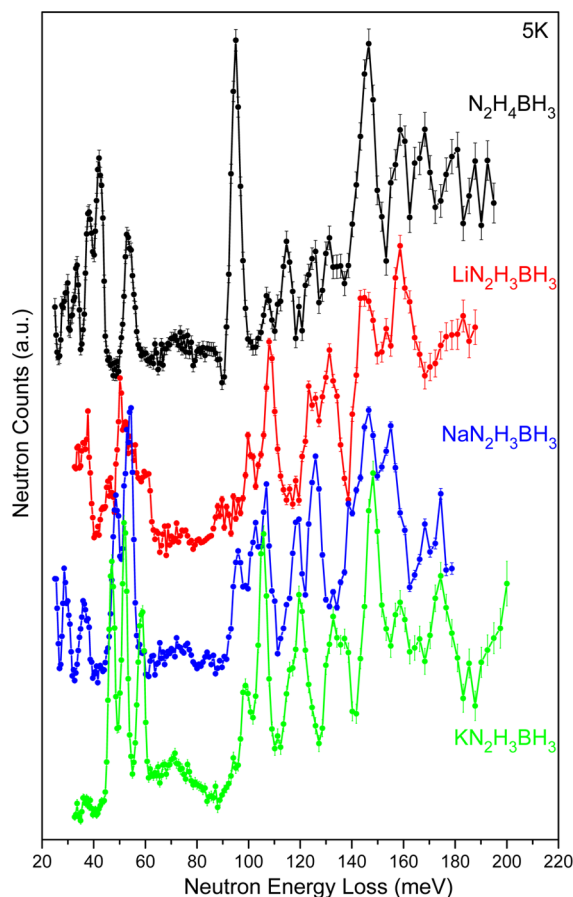


Figure 2. NVS analysis of $\text{MN}_2\text{H}_3\text{BH}_3$. NVS of pristine $\text{N}_2\text{H}_4\text{BH}_3$ was included for comparison.

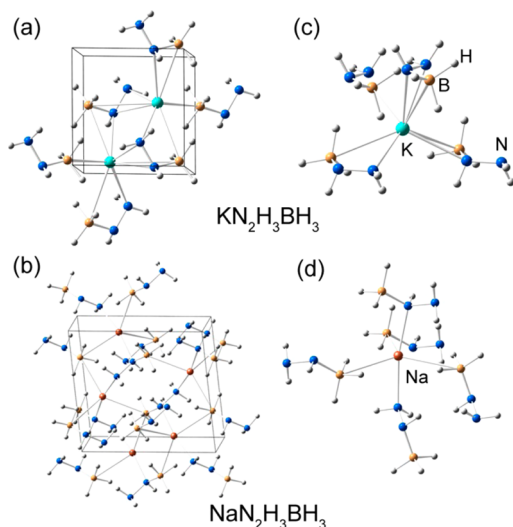


Figure 3. Crystal structures and cation coordination environments of $\text{KN}_2\text{H}_3\text{BH}_3$ (a, c) and $\text{NaN}_2\text{H}_3\text{BH}_3$ (b, d).

relaxed structure of $\text{NaN}_2\text{H}_3\text{BH}_3$ and $\text{KN}_2\text{H}_3\text{BH}_3$. Similar to that of $\text{LiN}_2\text{H}_3\text{BH}_3$, the hydridic hydrogen on the metal hydride reacts selectively with the protic hydrogen on internal nitrogen, releasing H_2 concurrently with the formation of an ionic bond between the metal cation and the nitrogen atom. Significantly, the substitution of a $\text{H}^{\delta+}$ with a metal cation transforms a molecular compound into an ionic compound. In this process,

the backbone of N–N–B remains intact and the tetrahedral coordination of the internal N is retained. Compared to $\text{N}_2\text{H}_4\text{BH}_3$, which contains only dihydrogen bond ($\text{N}-\text{H}^{\delta+}\cdots\delta^-\text{H}-\text{B}$) and hydrogen bond (terminal $\text{N}\cdots\delta^+\text{H}-\text{N}$) within its structure, the presence of M^+ in $\text{MN}_2\text{H}_3\text{BH}_3$ has induced reorientation of $[\text{NH}_2-\text{NH}-\text{BH}_3]^-$ anions that involves more complex interactions with M^+ . In $\text{NaN}_2\text{H}_3\text{BH}_3$, in addition to the direct ionic bonding between Na^+ and internal N with a bond distance of 2.431 Å, Na^+ also coordinates with three BH_3 groups in the same plane via $\text{Na}\cdots\text{H}^{\delta-}$ coordinations. Another $[\text{NH}_2-\text{NH}-\text{BH}_3]^-$ anion on the other side of the BH_3 tricoordinated plane also coordinates to Na^+ via lone pair of electrons from its terminal N, completing the Na^+ coordination sphere to form a trigonal bipyramid. As shown in Figure 3a,c, in $\text{KN}_2\text{H}_3\text{BH}_3$, K^+ is surrounded by four $[\text{NH}_2-\text{NH}-\text{BH}_3]^-$ anions. Because of the larger ionic radius for K^+ than for Na^+ , the K^+ cation interacts more intimately with surrounding ionic species than Na^+ . K^+ directly interacts with two internal N ($\text{K}-\text{N}$ ionic bonds), lone pair electrons of two terminal N ($\text{K}\cdots\text{N}$ coordinations), and four BH_3 groups (via $\text{K}\cdots\text{H}^{\delta-}$ coordinations) from the surrounding $[\text{NH}_2-\text{NH}-\text{BH}_3]^-$ anions. Besides close interactions with metal cation, $[\text{NH}_2-\text{NH}-\text{BH}_3]^-$ anions also establish intermolecular dihydrogen interactions among themselves. The dihydrogen bonds in $\text{NaN}_2\text{H}_3\text{BH}_3$ and $\text{KN}_2\text{H}_3\text{BH}_3$ were detected with bond distances in the range of 2.273–2.391 and 1.947–2.131 Å, respectively. The interatomic bond distances of the calculated $\text{NaN}_2\text{H}_3\text{BH}_3$ and $\text{KN}_2\text{H}_3\text{BH}_3$ are shown in Table S3. It is noteworthy that the smaller the ionic radius of the alkali metal cation, the more polarized the $[\text{NH}_2-\text{NH}-\text{BH}_3]^-$ anion. ^{11}B solid state NMR characterizations on the $\text{LiN}_2\text{H}_3\text{BH}_3$, $\text{NaN}_2\text{H}_3\text{BH}_3$, and $\text{KN}_2\text{H}_3\text{BH}_3$ (Figure 4) showed an sp^3 boron resonance at

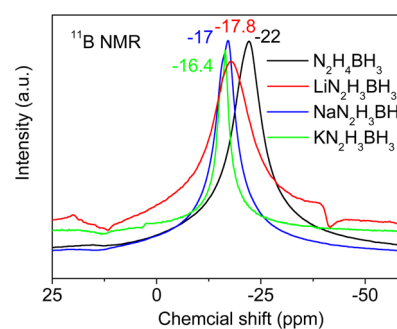


Figure 4. ^{11}B solid state MAS NMR characterization of $\text{LiN}_2\text{H}_3\text{BH}_3$, $\text{NaN}_2\text{H}_3\text{BH}_3$, and $\text{KN}_2\text{H}_3\text{BH}_3$. $\text{N}_2\text{H}_4\text{BH}_3$ was also included for comparison.

–17.8, –17.0, and –16.4 ppm, respectively, which has downfield shifted compared to the –22 ppm resonance found in pristine $\text{N}_2\text{H}_4\text{BH}_3$. It is clear that the sp^3 resonance is more downfield shifted with increasing cation size, an evidence of a variation in the polarizing power of metal cations with different ionic radii. A similar phenomenon was observed in the metal hydride modification of ammonia borane, where the change of a substituent at the nitrogen position affects the electron distribution of the molecule.^{4,14,15}

From the structural analyses, it can be seen that the N–N bonds in both $\text{NaN}_2\text{H}_3\text{BH}_3$ (1.461 Å) and $\text{KN}_2\text{H}_3\text{BH}_3$ (1.463 Å) are shortened by ca. 0.01 Å compared to that found in $\text{N}_2\text{H}_4\text{BH}_3$, whereas the B–N bonds are shortened from 1.596 Å

(in $\text{N}_2\text{H}_4\text{BH}_3$)⁸ to 1.540 Å (in $\text{NaN}_2\text{H}_3\text{BH}_3$) and 1.541 Å (in $\text{KN}_2\text{H}_3\text{BH}_3$). The structure and bonding environment of $\text{MN}_2\text{H}_3\text{BH}_3$ are further investigated and supported by neutron vibrational spectroscopy (see Figure 2 and Figure S7). Compared to the B–N and N–N collective stretching modes of pristine $\text{N}_2\text{H}_4\text{BH}_3$ (95 meV), those modes in $\text{MN}_2\text{H}_3\text{BH}_3$ all shift toward higher energy range (98–118 meV). In addition, FTIR (Figure S8) results showed a lesser N–H expressions in the range of 2600–3400 cm^{-1} in $\text{NaN}_2\text{H}_3\text{BH}_3$ and $\text{KN}_2\text{H}_3\text{BH}_3$ than that of $\text{N}_2\text{H}_4\text{BH}_3$. Red-shifts of B–H vibrations in the range of 1850–2500 cm^{-1} were clearly seen in $\text{NaN}_2\text{H}_3\text{BH}_3$ and $\text{KN}_2\text{H}_3\text{BH}_3$ compared to $\text{N}_2\text{H}_4\text{BH}_3$. The red-shift of B–H bonds can be ascribed to the $\text{M}^+\cdots\text{H}_3\text{B}$ interactions and the intermolecular dihydrogen bonding between $\text{H}^{\delta-}$ on B and the $\text{H}^{\delta+}$ on terminal or internal N from the neighboring molecules. Both forces can substantially lengthen the B–H bonds in $\text{MN}_2\text{H}_3\text{BH}_3$, $\text{LiN}_2\text{H}_3\text{BH}_3$, which is in the same family, also exhibited a wider range of B–H vibrations with slight red-shift, as a result of the extended dihydrogen bonding network.⁸

From these results, it is clear that the bonding chemistry of $\text{MN}_2\text{H}_3\text{BH}_3$ has changed significantly compared to pristine $\text{N}_2\text{H}_4\text{BH}_3$. Earlier investigations on metal amidoboranes showed that substantial changes in the various bond strengths in NH_3BH_3 have led to significant variations in the dehydrogenation behavior.^{4,15,16} Therefore, it is worthwhile to investigate the dehydrogenation performances of alkali-metal-modified $\text{N}_2\text{H}_4\text{BH}_3$ and study the influence and correlation of different metal cations toward dehydrogenation profiles of $\text{MN}_2\text{H}_3\text{BH}_3$. In order to evaluate the dehydrogenation performance of $\text{MN}_2\text{H}_3\text{BH}_3$ (M = Li, Na, and K), open system dehydrogenation (i.e., TPD-MS and TG-DTA) and closed system dehydrogenation (i.e., volumetric release and C80 calorimetric measurements) were conducted and compared with those for pristine $\text{N}_2\text{H}_4\text{BH}_3$.

As shown in Figure 5, TPD-MS results of $\text{NaN}_2\text{H}_3\text{BH}_3$ and $\text{KN}_2\text{H}_3\text{BH}_3$ demonstrated a two-step dehydrogenation profile,

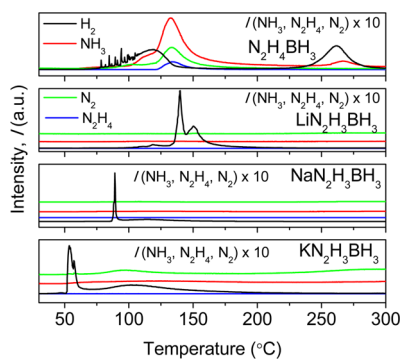


Figure 5. TPD-MS measurements on $\text{LiN}_2\text{H}_3\text{BH}_3$, $\text{NaN}_2\text{H}_3\text{BH}_3$, and $\text{KN}_2\text{H}_3\text{BH}_3$. TPD of $\text{N}_2\text{H}_4\text{BH}_3$ was also included for comparison.

with more rapid kinetics in the first step than the latter step. For $\text{NaN}_2\text{H}_3\text{BH}_3$, the first dehydrogenation step peaked at 89 °C, followed by a broad hump covering from 95 to 150 °C in the second step. This result agrees with that reported by Moury et al.⁹ A negligible amount of NH_3 and N_2 can be detected upon increasing their intensities by a factor of 10. Likewise in $\text{KN}_2\text{H}_3\text{BH}_3$, the first step peaked at 52 °C and a wider second step covered from 62 to 150 °C. A small shoulder peak aroused at 57 °C as a result of the sample foaming. However, the dehydrogenation was accompanied by a small amount of NH_3

and N_2 . $\text{LiN}_2\text{H}_3\text{BH}_3$, on the other hand, demonstrated three steps dehydrogenation, with a small amount of H_2 release in the first step followed by two major dehydrogenation profiles at 140 and 150 °C, agreeing with that reported in the literature.⁸ Both open system and closed system calorimetric measurements, i.e., TG-DTA (Figure 6) and C80 (Figure S9), showed

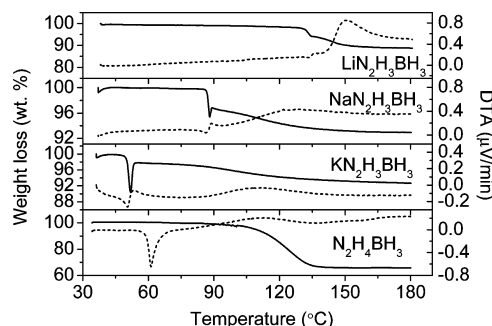


Figure 6. TG-DTA measurements on $\text{LiN}_2\text{H}_3\text{BH}_3$, $\text{NaN}_2\text{H}_3\text{BH}_3$, and $\text{KN}_2\text{H}_3\text{BH}_3$. TG-DTA of $\text{N}_2\text{H}_4\text{BH}_3$ was also included for comparison.

that $\text{N}_2\text{H}_4\text{BH}_3$, $\text{NaN}_2\text{H}_3\text{BH}_3$, and $\text{KN}_2\text{H}_3\text{BH}_3$ underwent an endothermic process prior to major decomposition. The endothermic phenomenon in $\text{N}_2\text{H}_4\text{BH}_3$ was ascribed to the melting of the sample.⁷ Similarly, we visually observed the melting process in $\text{NaN}_2\text{H}_3\text{BH}_3$ and $\text{KN}_2\text{H}_3\text{BH}_3$ at ca. 75 and 40 °C, respectively. TG results showed that $\text{NaN}_2\text{H}_3\text{BH}_3$ and $\text{KN}_2\text{H}_3\text{BH}_3$ share a unique property—the first step of mass loss is always followed by a weight gain. This buoyancy issue has also been reported in the decomposition of ammonia borane derivatives.¹⁷ For $\text{MN}_2\text{H}_3\text{BH}_3$, the melting phenomenon prior to the rapid dehydrogenation is likely to be the main reason for the buoyancy issue as the formation of H_2 bubbles in the melted samples was clearly observed under a microscope. Because of the relatively low density of H_2 compared to the Ar carrier gas, it is possible that H_2 bubbles could “lift up” the melted sample which would be interpreted as a larger than expected mass loss. As dehydrogenation proceeds, the melt solidifies and the H_2 bubbles disappear, resulting in an apparent weight gain in the TG profile. From the TG results, it is clearly shown that $\text{NaN}_2\text{H}_3\text{BH}_3$ and $\text{KN}_2\text{H}_3\text{BH}_3$ underwent mass losses of ca. 3.2% and 2.2%, respectively, disregarding the buoyancy effect in the first step. Increasing the temperature to 180 °C resulted in total mass losses of ca. 7.1% and 7.3%, respectively. However, $\text{N}_2\text{H}_4\text{BH}_3$ underwent significant mass loss of 33.7% in the temperature range of 90–140 °C, releasing a considerable amount of heavy gaseous products other than H_2 , i.e., N_2H_4 , NH_3 , and N_2 . From the TPD-MS and TG-DTA analyses, improvements in view of the dehydrogenation temperature and hydrogen purity are magnificent in metal hydrazidodihydroborates.

Different from the dynamic flow mode (open system) of TG-DTA and TPD-MS measurements, a closed system volumetric release measurement enables the gaseous product to be trapped in a confined space and allow it to further participate in the secondary reaction.¹⁸ Therefore, the dehydrogenation behavior of a closed system may differ compared to that of an open system. A closed system volumetric release measurement of $\text{N}_2\text{H}_4\text{BH}_3$ (Figure 7) showed a release of 2.1 equiv of gaseous product upon heating to 193 °C. This result is significantly different from an open system dehydrogenation whereby $\text{N}_2\text{H}_4\text{BH}_3$ released only ~1.0 equiv of H_2 at temperatures

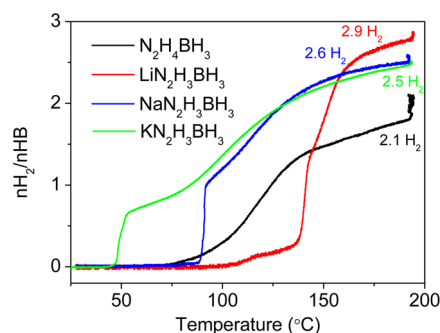


Figure 7. Closed system volumetric measurements on $\text{N}_2\text{H}_4\text{BH}_3$, $\text{LiN}_2\text{H}_3\text{BH}_3$, $\text{NaN}_2\text{H}_3\text{BH}_3$, and $\text{KN}_2\text{H}_3\text{BH}_3$ at a ramping rate of $2\text{ }^\circ\text{C}/\text{min}$.

between 100 and $150\text{ }^\circ\text{C}$.⁸ Under the closed condition, N_2H_4 and NH_3 formed in the decomposition may further participate in the dehydrogenation process to release more H_2 . It is clearly evidenced by MS analyses (Figure S10) that only NH_3 and N_2 were detectable in the gaseous product in addition to H_2 . Under the same conditions, $\text{LiN}_2\text{H}_3\text{BH}_3$, $\text{NaN}_2\text{H}_3\text{BH}_3$, and $\text{KN}_2\text{H}_3\text{BH}_3$, (Figure 7) released ca. 1.5, 1, and 0.7 equiv of gaseous product in the first step. Further increasing the temperature to $193\text{ }^\circ\text{C}$ resulted in a total release of 2.9, 2.6, and 2.5 equiv of gaseous product, respectively. In addition to the dominant H_2 signal, a small signal of N_2 can also be detected (Figure S10).

To shine a light on the kinetic improvement in the dehydrogenation of $\text{MN}_2\text{H}_3\text{BH}_3$, isothermal heating of various $\text{MN}_2\text{H}_3\text{BH}_3$ and $\text{N}_2\text{H}_4\text{BH}_3$ was carried out at $88\text{ }^\circ\text{C}$. As shown in Figure S11, approximately 1.5 equiv of H_2 (50% of its theoretical H, 4.5 wt %) and 1.8 equiv of H_2 (60% of its theoretical H, 4.3 wt %) can be released within 1 h from $\text{NaN}_2\text{H}_3\text{BH}_3$ and $\text{KN}_2\text{H}_3\text{BH}_3$, respectively. Under similar conditions, $\text{N}_2\text{H}_4\text{BH}_3$ released only 0.5 equiv of H_2 (15% of its theoretical H). These improvements imply a greatly reduced energy barrier in the dehydrogenation of $\text{MN}_2\text{H}_3\text{BH}_3$ compared to that of $\text{N}_2\text{H}_4\text{BH}_3$.

Several pronounced improvements in the dehydrogenation properties of $\text{MN}_2\text{H}_3\text{BH}_3$ compared to $\text{N}_2\text{H}_4\text{BH}_3$ were observed as results of the substitution of $\text{H}^{\delta+}$ in $\text{N}_2\text{H}_4\text{BH}_3$ with an alkali metal cation, M^+ . For instances, inhibition of N_2H_4 and NH_3 during dehydrogenation and improved dehydrogenation kinetics. From the structural point of view, the presence of electropositive alkali metal cation not only strengthens the B–N and N–N bonds of $[\text{NH}_2\text{--NH--BH}_3]^-$ anion but also activates its B–H bonds via formation of intermolecular $\text{M}^+\cdots\text{H}^{\delta-}\text{--B}$ interactions. Such $\text{M}^+\cdots\text{H}^{\delta-}\text{--B}$ interactions become stronger as the ionic character of the metal cation increases moving down the group, resulting in different extents of the B–H bond weakening. In other words, the polarizability of the B–N, N–N, and B–H bonds in $\text{N}_2\text{H}_4\text{BH}_3$ increase as an influence of the electron-donating metal cation. Owing to the analogous configurations of $\text{MN}_2\text{H}_3\text{BH}_3$ with that of MNH_2BH_3 , it is thus plausible to hypothesize a similar metal hydride mediated dehydrogenation pathway in the dehydrogenation of $\text{MN}_2\text{H}_3\text{BH}_3$.^{19–21} Under this proposed pathway, the hydridic $\text{H}^{\delta-}$ transfers from B to metal cation to form M--H prior to combining with protonic $\text{H}^{\delta+}$ to form H_2 . Apart from the improved dehydrogenation behavior, melting-induced decomposition was clearly observed in $\text{NaN}_2\text{H}_3\text{BH}_3$ and $\text{KN}_2\text{H}_3\text{BH}_3$. A lower melting point of

$\text{KN}_2\text{H}_3\text{BH}_3$ than $\text{NaN}_2\text{H}_3\text{BH}_3$ suggests that the melting is metal cation dependent. Because of the fact that the strength of intermolecular/atomic forces (i.e., $\text{M}\cdots\text{H}^{\delta-}\text{--B}$, $\text{M}\cdots\text{NH}_2$ and $\text{N--H}^{\delta+}\cdots\text{H}^{\delta-}\text{--B}$) determines the melting point of a compound, a molecule with larger metal cation tends to have weaker interaction with surrounding ligands. As a rapid dehydrogenation occurs simultaneously upon melting, it is reasonable to deduce an increasing ionic mobility in $\text{MN}_2\text{H}_3\text{BH}_3$ during the melting which is sufficient to overcome the kinetic barrier of the first step dehydrogenation.

To further elucidate the dehydrogenation mechanism, each $\text{MN}_2\text{H}_3\text{BH}_3$ sample was characterized at different heating stages (Figure S12) using ^{11}B solid state NMR, XRD, and FTIR. The powder X-ray diffraction patterns of the post-dehydrogenated samples did not show any peaks, which is an indication of the amorphous nature of the dehydrogenated products. The local B coordination geometry was also characterized with the aid of the solid state ^{11}B MAS NMR. As shown in Figure S13, three main boron species were detected in all metal hydrazidetrihydrioborates upon the first step dehydrogenation. A resonance with the chemical shift in the range of -16 to -18 ppm can be ascribed to the terminal NBH_3 species. However, this resonance diminished upon heating to $193\text{ }^\circ\text{C}$. Two additional broad resonances in the ranges of -3 to 10 ppm and 10 to 38 ppm which were not observed in the fresh sample (see Figure 4 and Figure S13) grew upon the first step dehydrogenation. At $193\text{ }^\circ\text{C}$, only the resonance in the range of $10\text{--}38$ ppm was observable. This resonance can be assigned to the tricoordinated sp^2 B species such as BN_3 or N_2BH , whereas the resonance in the range of -3 to 10 ppm can be ascribed to the intermediate tetracoordinated B species such as N_2BH_2 . Furthermore, the $^1\text{H} \rightarrow ^{11}\text{B}$ cross-polarization (CP) MAS characterizations indicate that both of these boron species are close to hydrogen, suggesting the presence of N_2BH_2 and N_2BH in the intermediate and only N_2BH in the product. In the post-dehydrogenated $\text{NaN}_2\text{H}_3\text{BH}_3$ and $\text{KN}_2\text{H}_3\text{BH}_3$, a very weak boron resonance was found in the range of -35 to -45 ppm in the $^1\text{H} \rightarrow ^{11}\text{B}$ CP MAS measurement. This peak is a characteristic resonance of sp^3 $[\text{BH}_4]^-$. Therefore, it is likely that a side reaction may have occurred in the dehydrogenation process, leading to the formation of $[\text{BH}_4]^-$ species. A similar observation was also reported by Moury et al.⁹ in $\text{NaN}_2\text{H}_3\text{BH}_3$ and by Grochala et al.²² in NaNH_2BH_3 . FTIR characterizations on the samples collected at different stages of closed system thermal treatment showed that N–H, B–H, B–N, and N–N vibrations were still clearly observed upon the first step dehydrogenation (Figure S14). Upon heating to $193\text{ }^\circ\text{C}$, only N–H, B–H, and B–N were detectable. Based on the information obtained from solid state NMR and FTIR characterizations, it is likely that $\text{MN}_2\text{H}_3\text{BH}_3$ polymerizes by intermolecular interaction between $\text{H}^{\delta+}$ in one molecule and $\text{H}^{\delta-}$ in the adjacent molecule in the early stage of dehydrogenation. Mulliken charge analysis in $\text{LiN}_2\text{H}_3\text{BH}_3$ evidenced a higher acidic nature of the $\text{H}^{\delta+}$ on terminal N in $\text{MN}_2\text{H}_3\text{BH}_3$.⁸ Therefore, although there is no direct evidence indicating which $\text{H}^{\delta+}$ is initially involved in the dehydrogenation (either $\text{H}^{\delta+}$ on internal N or terminal N), the higher acidic nature of the $\text{H}^{\delta+}$ on terminal N in $\text{MN}_2\text{H}_3\text{BH}_3$ suggests that it is more preferable to undergo deprotonation to release H_2 , forming possible species of $\text{NH}_2\text{NH}(\text{M})\text{BH}_2\text{NHNH}(\text{M})\text{BH}_3$ and $\text{NH}_2\text{NH}(\text{M})\text{BH}=\text{NNH}(\text{M})\text{BH}_3$ in the initial step. Further polymerization may take place at higher temperatures, resulting in $[\text{N}_2\text{H}_x\text{BH}_x]^-$ product. Nevertheless, additional theoretical

study is needed in order to have a clear understanding of the dehydrogenation mechanism of $MN_2H_3BH_3$.

In summary, the family of metal hydrazidotrihydridoborate was successfully expanded with additions of two new compounds, $MN_2H_3BH_3$ ($M = Na$ and K), using the wet chemical synthesis method. The crystal structure of $KN_2H_3BH_3$ was successfully determined using combined X-ray diffraction and first-principles calculations. The dehydrogenation properties of this series of alkali metal hydrazidotrihydridoborates were systematically investigated. From the present experimental results, $MN_2H_3BH_3$ may possibly undergo a similar dehydrogenation pathway as that of MNH_2BH_3 .^{19,21} A correlation was clearly observed between hydrogen desorption temperature and the melting temperature of $MN_2H_3BH_3$. Metal hydrazidotrihydridoborate with a smaller cation radius carries stronger intermolecular forces within the structure and thus possesses a higher melting temperature. The first step dehydrogenation occurs simultaneously upon melting owing to the increased ionic/molecular mobility of $MN_2H_3BH_3$ in the melted form. Sample foaming is thus unavoidable. However, it is possible to avoid foaming by introducing a catalyst to enable dehydrogenation prior to melting.²³ Therefore, our next step study will be to focus on exploring a suitable catalyst to increase H_2 formation selectivity and avoid sample foaming.

■ ASSOCIATED CONTENT

■ Supporting Information

XRD and FTIR data of various $MN_2H_3BH_3$; crystallographic information files (CIF) and Rietveld fit of $NaN_2H_3BH_3$ and $KN_2H_3BH_3$; C80 calorimetric measurements of $MN_2H_3BH_3$; kinetic studies of $MN_2H_3BH_3$ at 88 °C; MS analyses of the gaseous product formed upon dehydrogenation; volumetric release measurements of $MN_2H_3BH_3$ upon first step dehydrogenation; FTIR and ¹¹B solid state MAS NMR characterizations on intermediates and end products of $MN_2H_3BH_3$. This material is available free of charge via the Internet at <http://pubs.acs.org>.

■ AUTHOR INFORMATION

■ Corresponding Authors

*E-mail cys@dicp.ac.cn (Y.S.C.).

*E-mail pchen@dicp.ac.cn (P.C.).

*E-mail huiwu@nist.gov (H.W.).

■ Notes

Certain commercial suppliers are identified in this paper to foster understanding. Such identification does not imply recommendation or endorsement by the NIST.

The authors declare no competing financial interest.

■ ACKNOWLEDGMENTS

The authors acknowledge the financial support from 973 (2010CB631304) Project and National Natural Science Foundation of China (51225206, U1232120, 10979051, 21273229, 51301161). Y.S.C. thanks NIST for supporting his one-year visit as a postdoctoral guest researcher. Y.S.C. also acknowledges China Postdoctoral Science Foundation for the project funding. This work was supported in part by DOE-EERE under Grant DE-EE0002978. The authors thank BL14B1 of Shanghai Synchrotron Radiation Facility (SSRF) for providing the beam time.

■ REFERENCES

- (1) Xiong, Z. T.; Yong, C. K.; Wu, G. T.; Chen, P.; Shaw, W.; Karkamkar, A.; Autrey, T.; Jones, M. O.; Johnson, S. R.; Edwards, P. P.; David, W. I. F. High-Capacity Hydrogen Storage in Lithium and Sodium Amidoboranes. *Nat. Mater.* **2008**, *7* (2), 138–141.
- (2) Diyabalanage, H. V. K.; Shrestha, R. P.; Semelsberger, T. A.; Scott, B. L.; Bowden, M. E.; Davis, B. L.; Burrell, A. K. Calcium Amidotrihydroborate: A Hydrogen Storage Material. *Angew. Chem., Int. Ed.* **2007**, *46* (47), 8995–8997.
- (3) Kang, X. D.; Fang, Z. Z.; Kong, L. Y.; Cheng, H. M.; Yao, X. D.; Lu, G. Q.; Wang, P. Ammonia Borane Destabilized by Lithium Hydride: An Advanced on-Board Hydrogen Storage Material. *Adv. Mater.* **2008**, *20* (14), 2756–+.
- (4) Wu, H.; Zhou, W.; Yildirim, T. Alkali and Alkaline-Earth Metal Amidoboranes: Structure, Crystal Chemistry, and Hydrogen Storage Properties. *J. Am. Chem. Soc.* **2008**, *130* (44), 14834–14839.
- (5) Hügler, T.; Kühnel, M. F.; Lentz, D. Hydrazine Borane: A Promising Hydrogen Storage Material. *J. Am. Chem. Soc.* **2009**, *131* (21), 7444–7446.
- (6) Goubeau, J.; Ricker, E. Borinhydrazin Und Seine Pyrolyseprodukte. *Z. Anorg. Allg. Chem.* **1961**, *310* (3), 123–142.
- (7) Moury, R.; Moussa, G.; Demirci, U. B.; Hannauer, J.; Bernard, S.; Petit, E.; van der Lee, A.; Miele, P. Hydrazine Borane: Synthesis, Characterization, and Application Prospects in Chemical Hydrogen Storage. *Phys. Chem. Chem. Phys.* **2012**, *14* (5), 1768–1777.
- (8) Wu, H.; Zhou, W.; Pinkerton, F. E.; Udovic, T. J.; Yildirim, T.; Rush, J. J. Metal Hydrazinoborane $LiN_2H_3BH_3$ and $LiN_2H_3BH_3 \cdot 2N_2H_4BH_3$: Crystal Structures and High-Extent Dehydrogenation. *Energy Environ. Sci.* **2012**, *5* (6), 7531–7535.
- (9) Moury, R.; Demirci, U. B.; Ichikawa, T.; Filinchuk, Y.; Chiriac, R.; van der Lee, A.; Miele, P. Sodium Hydrazinidoborane: A Chemical Hydrogen-Storage Material. *ChemSusChem* **2013**, *6* (4), 667–673.
- (10) Larson, A. C.; Von Dreele, R. B. General Structure Analysis System (Gsas). Los Alamos National Laboratory, Report Laur 86-748, 2004.
- (11) Paolo, G.; Stefano, B.; Nicola, B.; Matteo, C.; Roberto, C.; Carlo, C.; Davide, C.; Guido, L. C.; Matteo, C.; Ismaila, D.; Andrea Dal, C.; Stefano de, G.; Stefano, F.; Guido, F.; Ralph, G.; Uwe, G.; Christos, G.; Anton, K.; Michele, L.; Layla, M.-S.; Nicola, M.; Francesco, M.; Riccardo, M.; Stefano, P.; Alfredo, P.; Lorenzo, P.; Carlo, S.; Sandro, S.; Gabriele, S.; Ari, P. S.; Alexander, S.; Paolo, U.; Renata, M. W. Quantum Espresso: A Modular and Open-Source Software Project for Quantum Simulations of Materials. *J. Phys.: Condens. Matter* **2009**, *21* (39), 395502.
- (12) Car, R.; Parrinello, M. Unified Approach for Molecular Dynamics and Density-Functional Theory. *Phys. Rev. Lett.* **1985**, *55* (22), 2471–2474.
- (13) Kresse, G.; Furthmüller, J.; Hafner, J. Ab Initio Force Constant Approach to Phonon Dispersion Relations of Diamond and Graphite. *Europhys. Lett.* **1995**, *32* (9), 729.
- (14) Staubitz, A.; Robertson, A. P. M.; Manners, I. Ammonia-Borane and Related Compounds as Dihydrogen Sources. *Chem. Rev.* **2010**, *110* (7), 4079–4124.
- (15) Chua, Y. S.; Chen, P.; Wu, G.; Xiong, Z. Development of Amidoboranes for Hydrogen Storage. *Chem. Commun.* **2011**, *47* (18), 5116–5129.
- (16) Wu, H.; Zhou, W.; Pinkerton, F. E.; Meyer, M. S.; Yao, Q.; Gadipelli, S.; Udovic, T. J.; Yildirim, T.; Rush, J. J. Sodium Magnesium Amidoborane: The First Mixed-Metal Amidoborane. *Chem. Commun.* **2011**, *47* (14), 4102–4104.
- (17) Zhang, Q. G.; Tang, C. X.; Fang, C. H.; Fang, F.; Sun, D.; Ouyang, L. Z.; Zhu, M. Synthesis, Crystal Structure, and Thermal Decomposition of Strontium Amidoborane. *J. Phys. Chem. C* **2010**, *114* (3), 1709–1714.
- (18) Chua, Y. S.; Wu, G. T.; Xiong, Z. T.; He, T.; Chen, P. Calcium Amidoborane Ammoniate-Synthesis, Structure, and Hydrogen Storage Properties. *Chem. Mater.* **2009**, *21* (20), 4899–4904.
- (19) Kim, D. Y.; Lee, H. M.; Seo, J.; Shin, S. K.; Kim, K. S. Rules and Trends of Metal Cation Driven Hydride-Transfer Mechanisms in

Metal Amidoboranes. *Phys. Chem. Chem. Phys.* **2010**, *12* (20), 5446–5453.

(20) Kim, D. Y.; Singh, N. J.; Lee, H. M.; Kim, K. S. Hydrogen-Release Mechanisms in Lithium Amidoboranes. *Chem.—Eur. J.* **2009**, *15* (22), 5598–5604.

(21) Lee, T. B.; McKee, M. L. Mechanistic Study of LiNH_2BH_3 Formation from $(\text{LiH})_4 + \text{NH}_3\text{BH}_3$ and Subsequent Dehydrogenation. *Inorg. Chem.* **2009**, *48* (16), 7564–7575.

(22) Fijakowski, K. J.; Grochala, W. Substantial Emission of NH_3 during Thermal Decomposition of Sodium Amidoborane, NaNH_2BH_3 . *J. Mater. Chem.* **2009**, *19* (14), 2043–2050.

(23) He, T.; Xiong, Z. T.; Wu, G. T.; Chu, H. L.; Wu, C. Z.; Zhang, T.; Chen, P. Nanosized Co- and Ni-Catalyzed Ammonia Borane for Hydrogen Storage. *Chem. Mater.* **2009**, *21* (11), 2315–2318.

Supporting Information

Alkali Metal Hydride Modification on Hydrazine Borane for Improved Dehydrogenation

Yong Shen Chua,^{a,b*} Qijun Pei,^c Xiaohua Ju,^a Wei Zhou,^{b,d} Terrence J. Udovic,^b Guotao Wu,^a
Zhitao Xiong,^a Ping Chen,^{a*} Hui Wu^{b,d*}

^aDalian National Laboratory for Clean Energy, Dalian Institute of Chemical Physics, Chinese Academy of Science, 457 Zhongshan Road, 116023, Dalian, China.

^bNIST Center for Neutron Research, National Institute of Standards and Technology, Gaithersburg, Maryland 20898-6102, United States.

^cSchool of Physical Science and Technology, Sichuan University, Chengdu 610065, China.

^dDepartment of Materials Science and Engineering, University of Maryland, College Park, Maryland 20742, United States.

Table S1. Experimental structural parameter of KN₂H₃BH₃ (Space group $P2_1$), $a = 6.72102$ (23) Å, $b = 5.89299$ (20) Å, $c = 5.77795$ (17) Å, $\beta = 108.2795$ (13) ° and $V = 217.298$ (15) Å³.

Atom	Site	x	y	z
H1	2a	0.06389	0.5611	0.2099
H2	2a	0.49598	0.3883	0.1716
H3	2a	0.19951	0.2701	0.9712
H4	2a	0.28984	0.6033	-0.0511
H5	2a	0.05693	0.1802	0.2794
H6	2a	0.12842	0.3083	0.5468
B7	2a	0.30694 (28)	0.4339 (28)	0.0806 (5)
N8	2a	0.20786 (28)	0.4836 (28)	0.2828 (5)
N9	2a	0.17787 (28)	0.2710 (28)	0.3992 (5)
K10	2a	0.43631 (24)	0.9213 (28)	0.28403 (26)

Table S2. Experimental structural parameter of $\text{NaN}_2\text{H}_3\text{BH}_3$ (Space group $P2_1/c$), $a = 4.97456$ (29) Å, $b = 7.9607$ (4) Å, $c = 10.2456$ (5) Å, $\beta = 115.1665$ (22) ° and $V = 367.22$ (4) Å³.

Atom	Site	x	y	z
B1	4e	0.3295 (8)	0.7592 (6)	0.53695 (35)
N2	4e	0.42721	0.69463	0.42211
N3	4e	0.2004 (5)	0.5934 (4)	0.31040 (29)
H4	4e	0.2270	0.6442	0.5866
H5	4e	0.5446	0.8238	0.63717
H6	4e	0.6073	0.61651	0.46728
H7	4e	0.0699	0.6740	0.23014
H8	4e	0.1314	0.8658	0.4836
H9	4e	0.0614	0.5436	0.3521
Na10	4e	0.6343(5)	0.90932 (28)	0.32615 (29)

* N2 position in $\text{NaN}_2\text{H}_3\text{BH}_3$ was set to be the centre of the $\text{N}_2\text{H}_3\text{BH}_3$ rigid body.

Table S3. Interatomic bond distances (Å) of the calculated $\text{NaN}_2\text{H}_3\text{BH}_3$ and $\text{KN}_2\text{H}_3\text{BH}_3$ crystal structures.

Bond Types	Bond Distances (Å)	
	$\text{NaN}_2\text{H}_3\text{BH}_3$	$\text{KN}_2\text{H}_3\text{BH}_3$
B-H	1.237-1.256	1.236-1.253
N-H	1.025-1.034	1.030-1.034
N-N	1.461	1.463
B-N	1.540	1.541
M-N	2.431	2.959-3.020
M...H	2.415-2.565	2.733-2.940
M...N	2.452	2.859-2.996
H...H	2.273-2.391	1.947-2.131

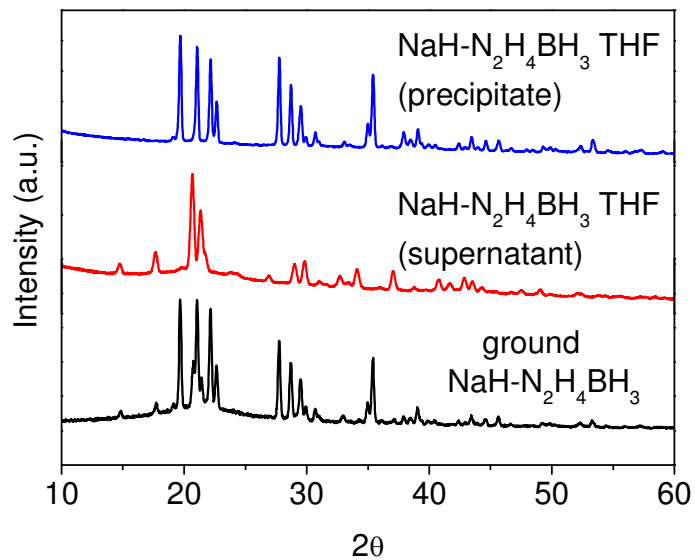


Figure S1. XRD pattern of the liquid state synthesized $\text{NaN}_2\text{H}_3\text{BH}_3$ (precipitate) and an unknown side product (supernatant). The XRD pattern of the hand ground $\text{NaN}_2\text{H}_3\text{BH}_3$ was included for comparison.

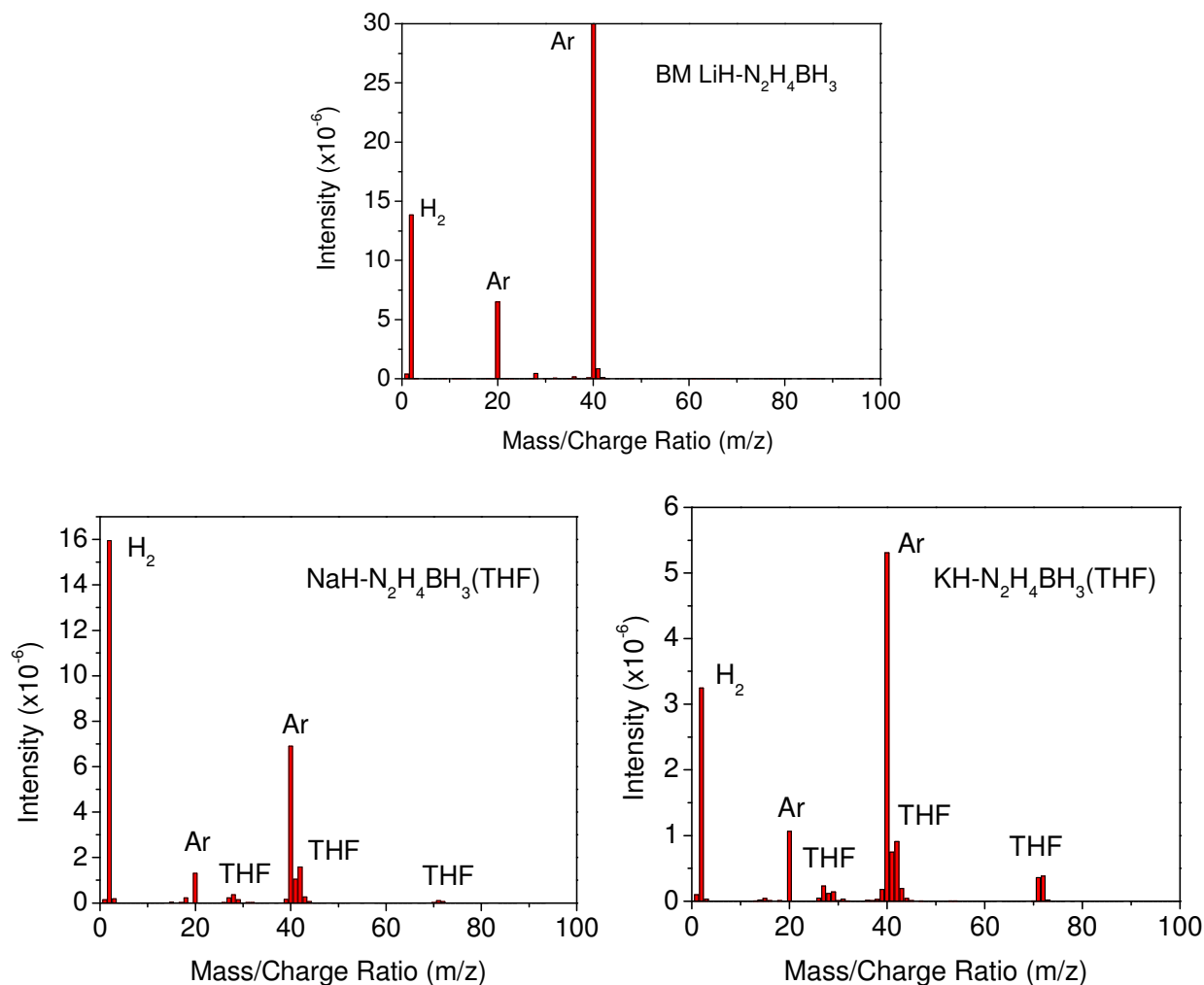


Figure S2. MS analyses of the gaseous product formed upon ball milling N₂H₄BH₃ and LiH, and interaction of N₂H₄BH₃ (THF) and NaH or KH in an autoclave. Signals of m/z ratio 15, 26, 27, 28, 29, 31, 39, 40, 41, 42, 43, 44, 71 and 72 corresponds to the fragments and parent signals of THF.¹ The strong argon gas (Ar) signal is originated from the glovebox during the sample loading.

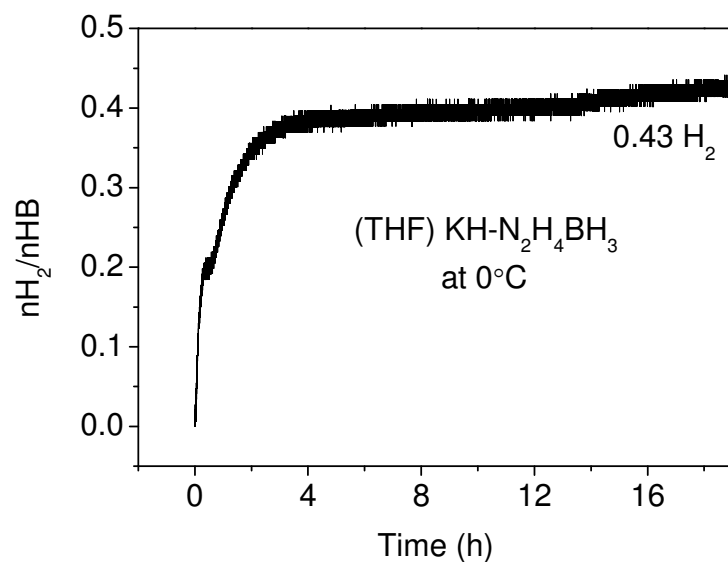


Figure S3. Time dependent pressure increase for $\text{KH-N}_2\text{H}_4\text{BH}_3$ (THF) at 0°C .

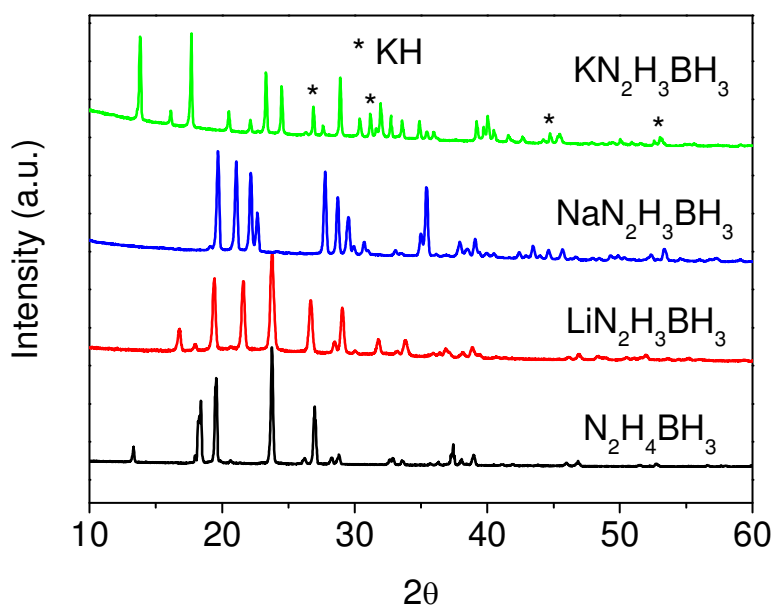


Figure S4. XRD patterns of the white powdery samples obtained from the ball milled $\text{LiH-N}_2\text{H}_4\text{BH}_3$ and liquid state interaction of $\text{NaH-N}_2\text{H}_4\text{BH}_3$ and $\text{KH-N}_2\text{H}_4\text{BH}_3$. XRD data of pristine $\text{N}_2\text{H}_4\text{BH}_3$ was included for comparison.

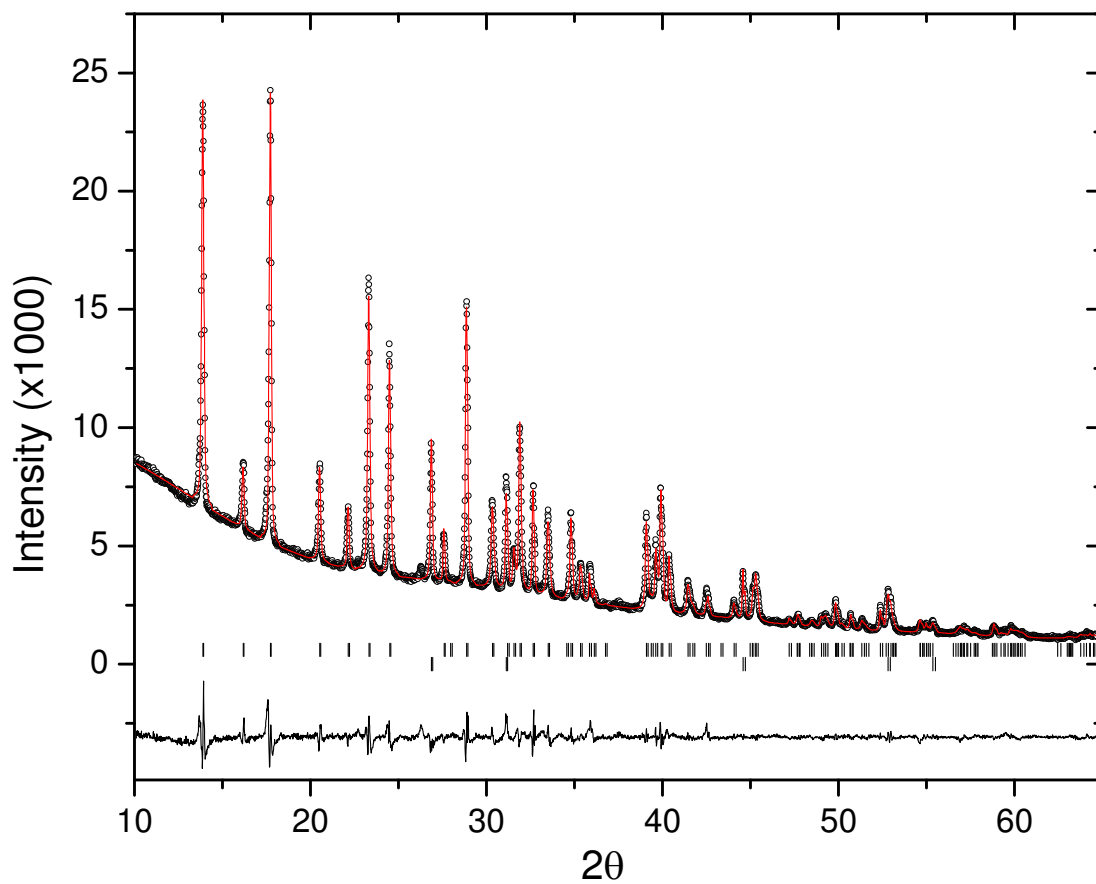


Figure S5. Experimental (circles), fitted (line), and difference (line below observed and calculated patterns) XRD profiles for $\text{KN}_2\text{H}_3\text{BH}_3$ at 298 K. Vertical bars indicate the calculated positions of Bragg peaks of $\text{KN}_2\text{H}_3\text{BH}_3$ and a slight amount of KH , respectively (from the top).

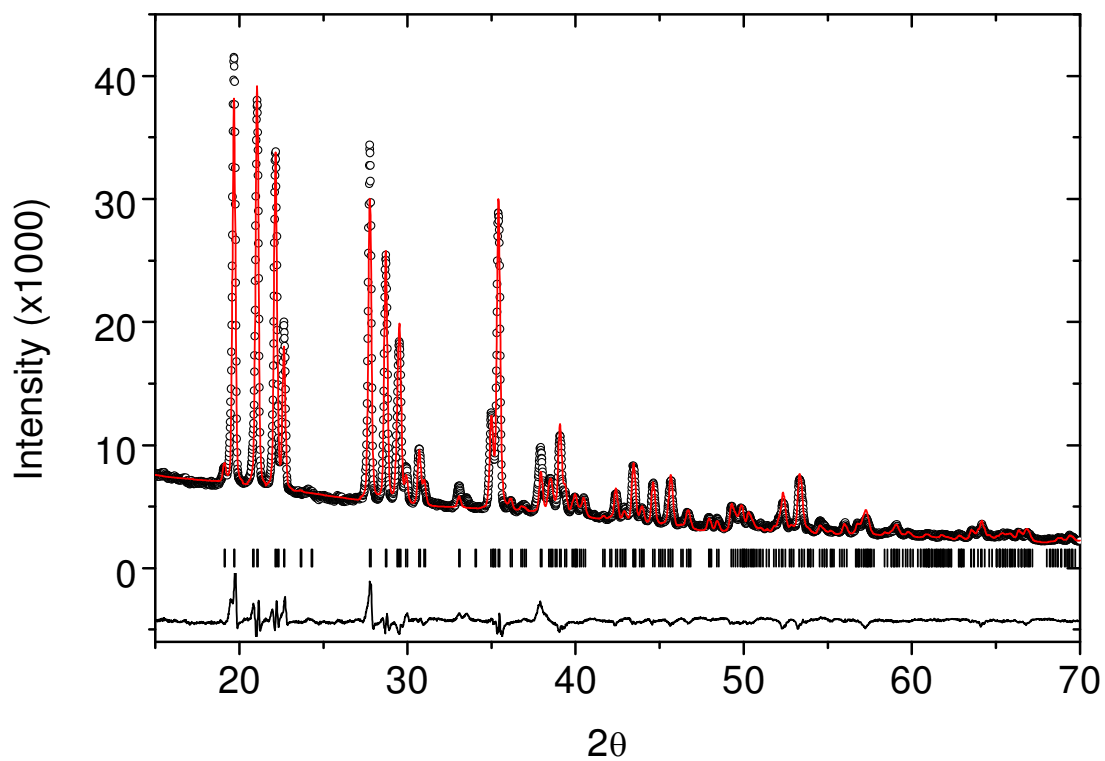


Figure S6. Experimental (circles), fitted (line), and difference (line below observed and calculated patterns) XRD profiles for $\text{NaN}_2\text{H}_3\text{BH}_3$ (synthesized via wet synthesis) at 298 K. Vertical bars indicate the calculated positions of Bragg peaks of $\text{NaN}_2\text{H}_3\text{BH}_3$.

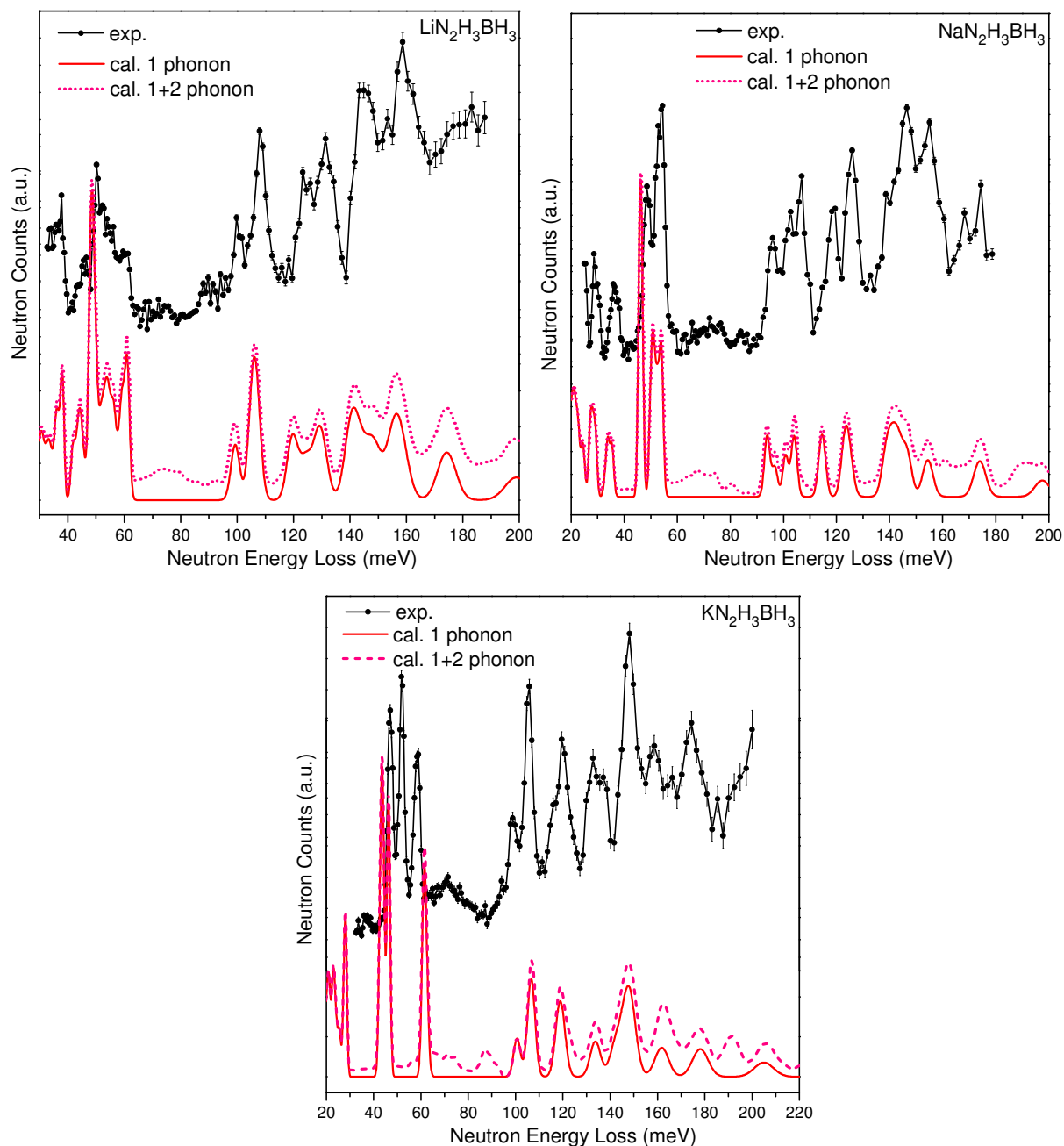


Figure S7 Observed and first-principles calculated neutron vibrational spectra of $\text{MN}_2\text{H}_3\text{BH}_3$. Error bars represent plus and minus the combined standard uncertainty.

The observed phonon bands can be assigned to the B-H and N-H collective rocking and librational modes of (40-60 meV), B-N and N-N collective stretching modes (98-110 meV), $\text{N}_2\text{H}_3\text{-BH}_3$ bending and wagging modes (110-140 meV), $\text{N}_2\text{H}_3\text{BH}_3^-$ deformation and torsion modes (140-150 meV), B-H scissoring modes (150-160 meV), internal N-H bending/wagging modes (170-180 meV), and terminal N-H scissoring modes (180-200 meV). In general, the calculated spectra agree well with the observed NV spectra, and thus further support the validity of the determined structures.

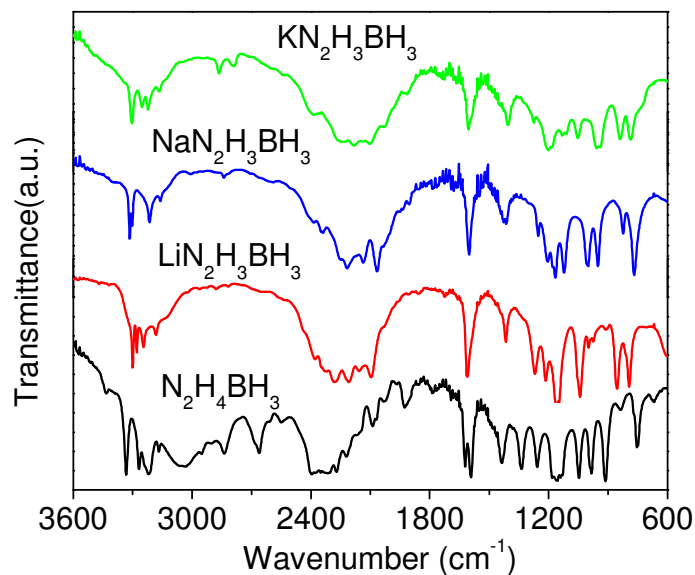


Figure S8. FTIR spectra of the white powdery samples obtained from the interaction of LiH-N₂H₄BH₃, NaH-N₂H₄BH₃, KH-N₂H₄BH₃ and pristine N₂H₄BH₃.

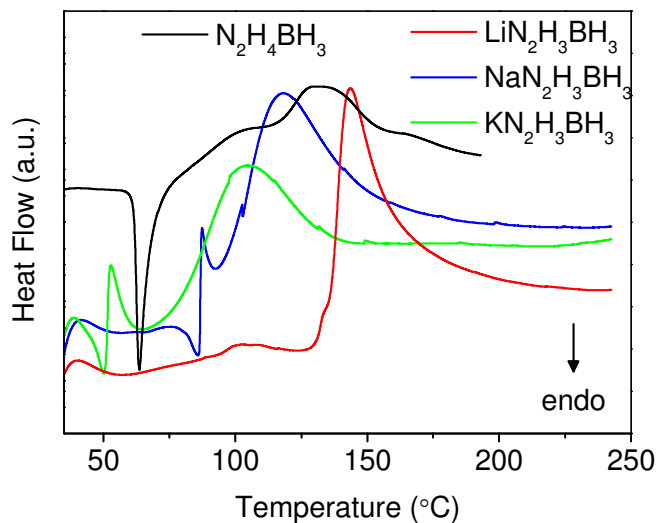


Figure S9. C80 calorimetric measurements of LiN₂H₃BH₃, NaN₂H₃BH₃ and KN₂H₃BH₃ at a ramping rate of 0.5 °C/min. N₂H₄BH₃ was also included for comparison.

An endothermic reaction is clearly observed in NaN₂H₃BH₃ and KN₂H₃BH₃ prior to an exothermic dehydrogenation process. Integrations of both endothermic and exothermic peaks were complicated by the overlaps of both signals. The melting endothermic peak of N₂H₄BH₃ was integrated to be 14.9 kJ/mol-HB, matching well with that reported by Moury et al.²

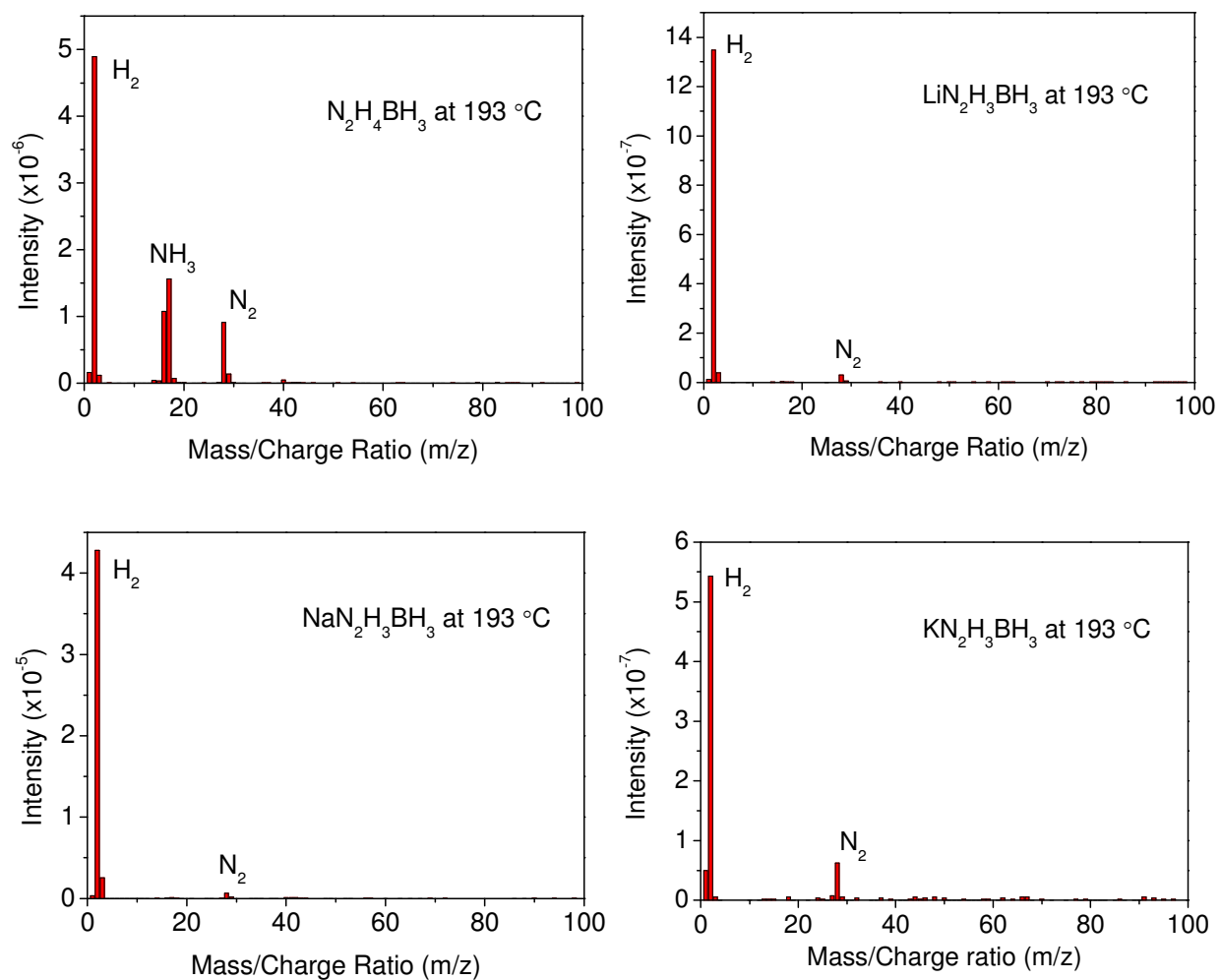


Figure S10. MS analyses of the gaseous product formed upon sample dehydrogenations at 193 °C in the closed-system.

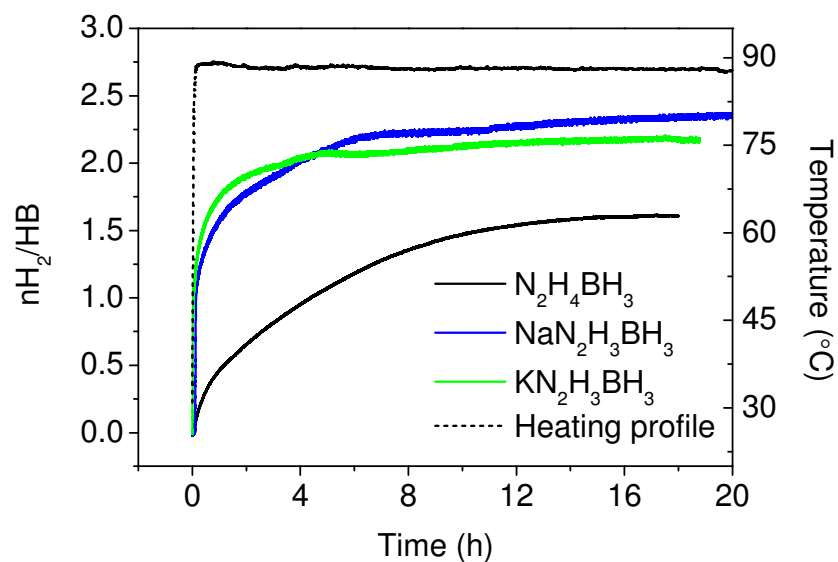


Figure S11. Kinetic studies of $\text{NaN}_2\text{H}_3\text{BH}_3$ and $\text{KN}_2\text{H}_3\text{BH}_3$ via isothermal heating at $88\text{ }^\circ\text{C}$. $\text{N}_2\text{H}_4\text{BH}_3$ was also included for comparison.

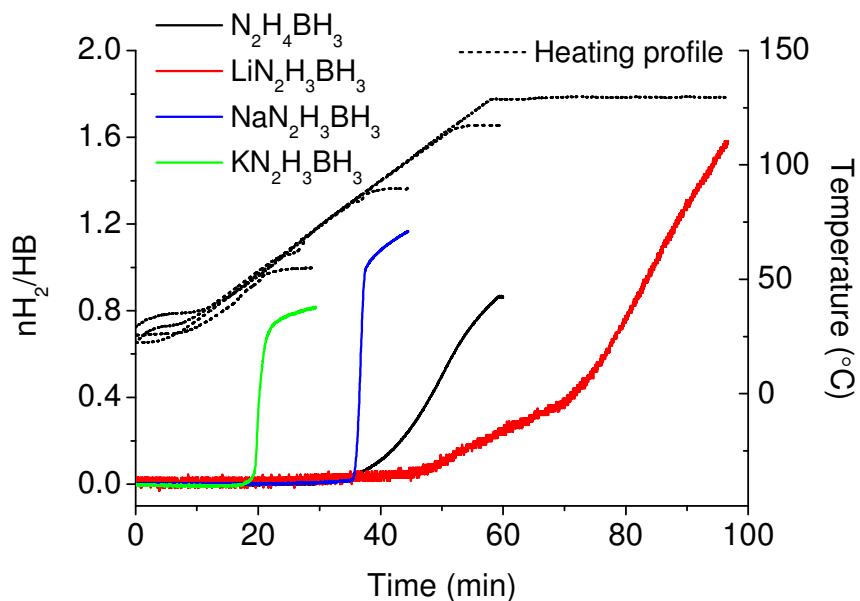


Figure S12. $\text{LiN}_2\text{H}_3\text{BH}_3$, $\text{NaN}_2\text{H}_3\text{BH}_3$ and $\text{KN}_2\text{H}_3\text{BH}_3$ were heated at a ramping rate of 2 Kmin^{-1} to $135\text{ }^\circ\text{C}$, $90\text{ }^\circ\text{C}$ and $55\text{ }^\circ\text{C}$ respectively, which correspond to the first step dehydrogenation in each sample. Dehydrogenation of $\text{N}_2\text{H}_4\text{BH}_3$ is not a stepwise process. However, $\text{N}_2\text{H}_4\text{BH}_3$ was collected at $120\text{ }^\circ\text{C}$ upon releasing ~ 0.9 equiv. of H_2 for comparison.

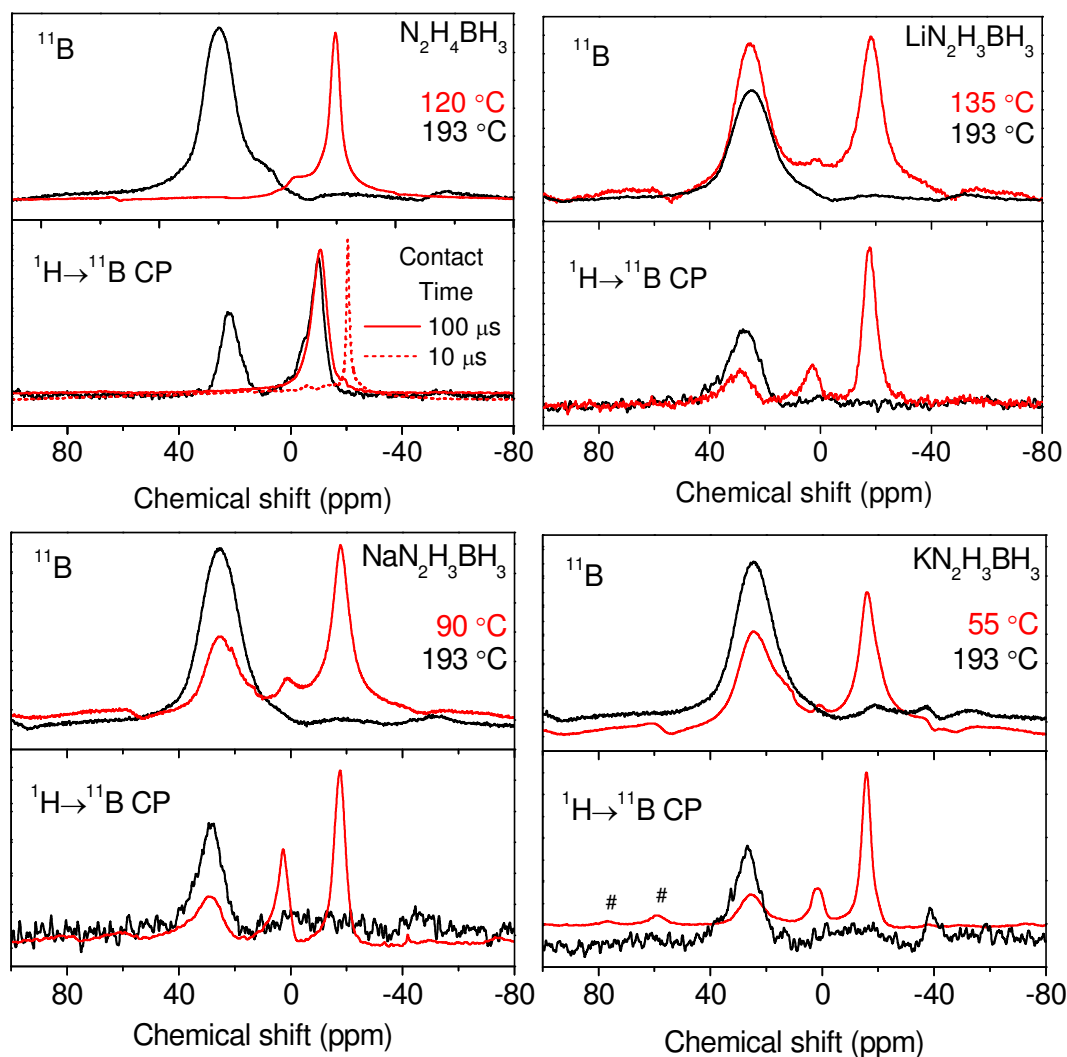


Figure S13. ^{11}B (Top) and $^1\text{H}\rightarrow^{11}\text{B}$ CP (Bottom) MAS solid state NMR characterizations of the samples collected at each step. The $\text{MN}_2\text{H}_3\text{BH}_3$ samples were heated at a ramping rate of $2\text{ }^\circ\text{Cmin}^{-1}$ to $55\text{ }^\circ\text{C}$, $90\text{ }^\circ\text{C}$ and $135\text{ }^\circ\text{C}$ respectively, which corresponds to the first step dehydrogenation in each sample. The intermediate sample of $\text{N}_2\text{H}_4\text{BH}_3$ at $120\text{ }^\circ\text{C}$ was also included for comparison. # denotes spinning side bands.

From the ^{11}B MAS NMR characterization of $\text{N}_2\text{H}_4\text{BH}_3$, it is clearly shown that at $120\text{ }^\circ\text{C}$, two boron environments can be detected; a shoulder resonance and an individual resonance peaked at -5.5 ppm and -19.5 ppm , respectively. $^1\text{H}\rightarrow^{11}\text{B}$ CP MAS measurements with different contact time showed two individual resonances at -10 ppm and -20 ppm , suggesting the presence of N_2BH_2 and terminal NBH_3 species. Experiments with different contact time were carried out because the cross polarization is based on $^{11}\text{B} - ^1\text{H}$ dipolar interactions and cross polarization kinetics varies with each type of B-H. No $\text{sp}^2\text{ N}_2\text{BH}$ or BN_3 species can be detected at this stage.

However, upon increasing the temperatures to 193 °C, a broad resonance which corresponds to N_2BH or BN_3 species can be detected. Interestingly, $^1H \rightarrow ^{11}B$ CP MAS measurement showed an additional signal at -10 ppm apart from the N_2BH peak in the range of 11 ppm to 29 ppm. The -10 ppm resonance can be attributed to the N_2BH_2 species which exists in relatively low concentration in the sample as there is no significant resonance that is observable in the same region in ^{11}B MAS NMR spectra.

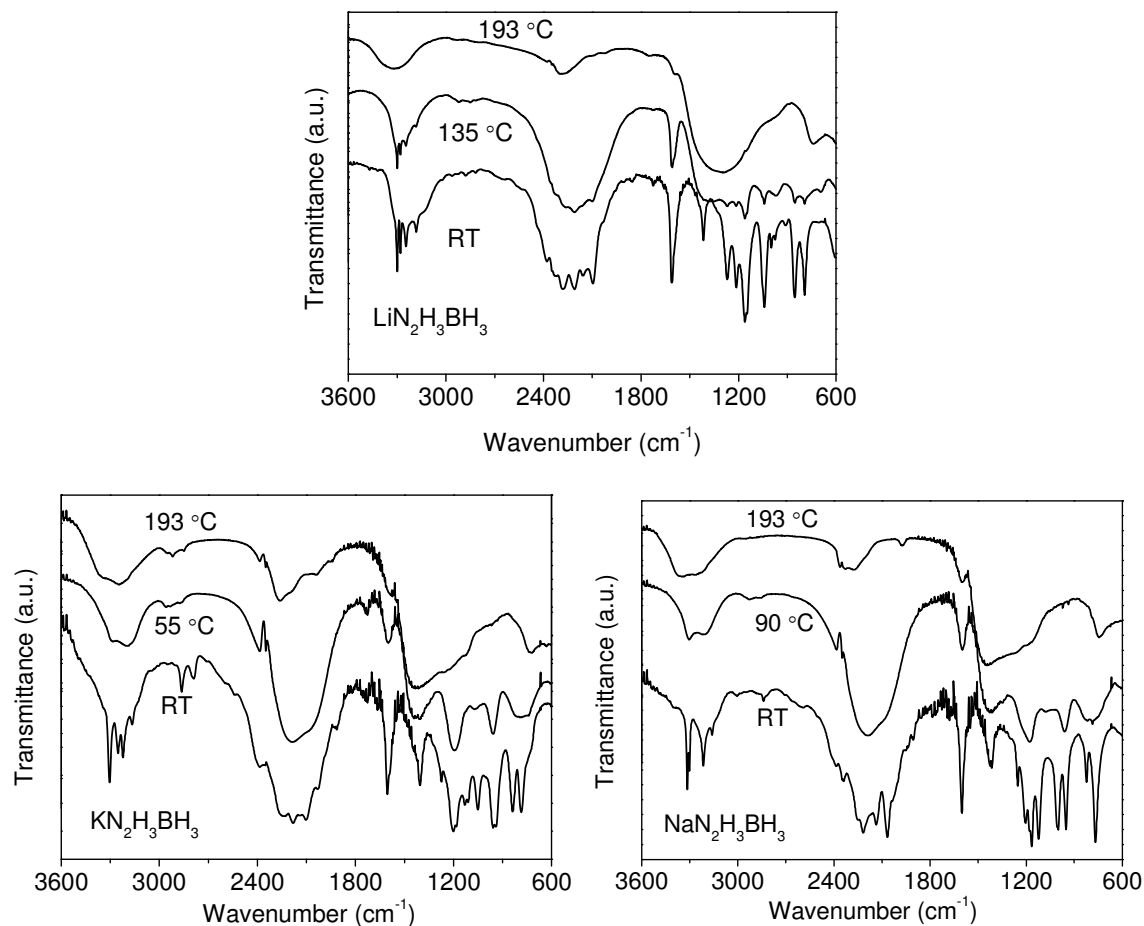


Figure S14. FTIR characterizations of the $LiN_2H_3BH_3$, $NaN_2H_3BH_3$ and $KN_2H_3BH_3$ collected at different stages of thermal treatment.

1. Marcin, D.; Ewelina, S.; Brygida, M.; Mariusz, Z., Ionization and Ionic Fragmentation of Tetrahydrofuran Molecules by Electron Collisions. *J. Phys. B: At. Mol. Opt. Phys.* **2011**, *44* (5), 055206.
2. Moury, R.; Moussa, G.; Demirci, U. B.; Hannauer, J.; Bernard, S.; Petit, E.; van der Lee, A.; Miele, P., Hydrazine Borane: Synthesis, Characterization, and Application Prospects in Chemical Hydrogen Storage. *Phys. Chem. Chem. Phys.* **2012**, *14* (5), 1768-1777.